

Diagenesis of magnetic minerals in a gas hydrate /cold seep environment off the Krishna-Godavari basin, Bay of Bengal

P. Dewangan^{1*}, N. Basavaiah², F. K. Badesab¹, A. Usapkar¹, A. Mazumdar¹, R. Joshi¹, and T. Ramprasad¹

¹CSIR-National Institute of Oceanography, Dona Paula, Goa-403004, India

²Indian Institute of Geomagnetism, Panvel, Navi Mumbai -410218, India

*for correspondence: pdewangan@nio.org

Abstract

We carried out detailed magnetic measurements of the core (MD161/8) located in the vicinity of Site NGHP-01-10, where ~128 m of hydrate is confirmed by drilling/coring, to understand the diagenesis of magnetic minerals in a gas hydrates/cold seep environment. The rock magnetic measurements along with SEM-EDS and XRD analyses show a zone of reduced magnetic susceptibility (*zone 2*) where most of the magnetic minerals are dissolved. The enhanced concentration of chromium reducible sulfur (CRS) in this zone suggests an intense pyritization process while isotopically depleted authigenic carbonates indicate sulfate reduction via anaerobic oxidation of methane (AOM). Therefore, the dissolution of magnetic minerals is attributed to the HS⁻ released during AOM that has resulted in the reduction in the magnitude of magnetic parameters.

Within zone 2, a zone of enhanced susceptibility (*zone 2a*) is observed between 17.68 and 23.6 mbsf, and is located beneath the present day sulfate-methane transition zone (SMTZ). The frequency-dependent magnetic susceptibility and low temperature magnetic measurements suggest the abundance of fine grained superparamagnetic (SP) sized ferrimagnetic particles. The SEM-EDS and XRD analyses show the presence of greigite which occurs in interstices between the pyrite crystals. Such occurrence of greigite in sediments has important implications in the interpretation of paleomagnetic records. We evaluated the likely mechanism for the greigite formation in KG offshore basin and our data suggest that the formation of greigite may be related to either paleo-SMTZ or anaerobic oxidation of pyrite. It is unlikely that the formation of greigite can be explained by the downward diffusion of sulfide below the current depth of SMTZ. However, further investigations are required to ascertain the mechanism for the formation and preservation of greigite.

Keywords: Magnetite dissolution, SP/SD size greigite, sediment diagenesis, sulfate reduction, anaerobic oxidation of methane

1. Introduction

The reductive dissolution of iron oxides and authigenic formation of magnetic minerals have been studied extensively in marine sediments as they have important implications for the interpretation of environmental and paleomagnetic records (e.g., Snowball and Thompson, 1990; Verosub and Roberts, 1995). In marine environment, iron and sulfur cycles are mostly mediated microbially by degradation of organic carbon (Froelich et al., 1979). Under suboxic conditions, authigenic magnetite of biogenic origin is commonly found at the top of the iron reduction zone (Lyle, 1983; Peterson et al., 1986; Karlin et al., 1987). Under anoxic conditions, the detrital iron-bearing minerals react with the hydrogen sulfide (HS^-) which is produced during anaerobic reduction of sulfate to form pyrite (FeS_2) (Karlin and Levi, 1983; Karlin and Levi, 1985; Canfield and Berner, 1987; Leslie et al., 1990; Karlin, 1990). As a precursor to pyrite, metastable greigite (Fe_3S_4) is formed during the pyritization process (Berner, 1984; Wilkins and Barnes, 1997; Hunger and Benning, 2007). If the pyritization process is incomplete either due to the limited concentration of hydrogen sulfide or enrichment of reactive iron, the intermediate ferrimagnetic iron sulfide (greigite) may be preserved in the marine sediments (Kao et al., 2004; Rowan and Roberts, 2006). Several studies have documented the presence of greigite formed due to sulfate reduction either by oxidation of organic matter (Liu et al., 2004) or anaerobic oxidation of methane (AOM) (Housen and Musgrave, 1996; Kasten et al., 1998; Liu et al., 2004; Neretin et al., 2004; Jørgensen et al., 2004; Horng and Chen, 2006; Musgrave et al., 2006; Larrasoana et al., 2006).

Greigite, a ferrimagnetic mineral capable of acquiring stable remanent magnetization, has received considerable attention due to its implications in paleomagnetic records (Jiang et al., 2001; Kao et al., 2004; Roberts et al., 2005; Rowan and Roberts, 2006; Larrasoana et al., 2007). The greigite lattice is similar to that of magnetite with higher coercivity, lower susceptibility and saturation magnetization (Robert, 1995). According to the steady-state diagenetic model (e.g., Berner, 1984), greigite is formed shortly after deposition and therefore accurately records the geomagnetic field at the time of its formation (Tric et al., 1991; Robert and Turner, 1993). However, recent studies have shown that the presence of authigenic SP/SD greigite can significantly overprint the paleomagnetic records (Kasten et al., 1998; Jiang et al., 2001; Jørgensen et al., 2004; Liu et al., 2004; Neretin et al., 2004; Robert and Weaver, 2005; Fu et al., 2008; Rowan et al., 2009). The processes for the formation of authigenic SP/SD greigite are not well studied in different geological environments. Therefore, we carried out detailed magnetic measurements along with SEM-EDS and XRD analyses on a long sediment core (~30 m) in which the evidence of paleo-cold seep activity has been reported (Mazumdar et al., 2009). The core was

collected onboard R/V *Marion Dufresne* (MD161/8) in the Krishna-Godavari (KG) offshore basin using a Giant Calypso piston corer with a PVC liner of 10 cm inner diameter at a water depth of 1033 m (Latitude =15° 51.8624'N and longitude = 81° 50.0692'E, Fig. 1a). The magnetic measurements vis-à-vis the geochemical and sedimentological data were analyzed to understand the effect of cold seep processes on the magnetic minerals.

2. Geological background

The study area lies in the KG basin which is a proven petroliferous basin located in the middle of the eastern continental margin of India (ECMI). The ECMI came into existence after the breakup of Gondwanaland around 130 Ma when India drifted away from East Antarctica (Powell et al., 1988; Scotese et al., 1988; Ramana et al., 1994). The KG basin extends from Ongole in the south to Vishakapatnam in the north and occupies an area of 28,000 sq. km onland and 145,000 sq. km offshore (Ojha and Dubey, 2006). Sediment thickness in the KG basin varies from 3-5 km in the onshore region to as much as 8 km in the offshore region (Prabhakar and Zutshi, 1993). The bulk of detrital sediments are carried by the Krishna and Godavari river systems along with their tributaries. The bulk of the sediment brought by these river systems consists of montmorillonite clay with traces of illite and kaolinite, while the Ganges-Brahmaputra river systems deposit sediments in the Bay of Bengal consisting of equal proportions of kaolinite, illite and chlorite (Subramanian, 1980). The Ganges-Brahmaputra sediments are coarse grained while the Krishna-Godavari sediments are fine grained, attributed to the differential settling mechanism as proposed by Gibbs (1977).

The pressure-temperature conditions in the KG offshore basin beyond 700 m water depths are suitable for the formation of gas hydrate, an ice-like crystalline solid which can trap methane gas within the cages of water molecules (Sloan, 1990). The seismic data show the regional presence of gas hydrate manifested in the form of bottom simulating reflectors (BSRs) in the KG offshore basin (Ramana et al., 2007; Collett et al., 2008). BSRs represent the phase boundary between the low velocity gas charged sediment and high velocity hydrate bearing sediment (Singh et al., 1993). Recent drilling/coring on board JOIDES Resolution has confirmed the presence of subsurface gas hydrate in KG offshore basin (Collett, et al., 2008). One of the drilled sites (NGHP-01-10) shows ~128 m thick subsurface gas hydrate of about 25-30 % saturation as estimated from the analysis of well-log data (Lee and Collett, 2009). The gas hydrate is observed from ~30 meters below seafloor (mbsf) to the base of the hydrate

stability zone i.e., ~160 mbsf. The location of the core (MD161/8) lies in the vicinity of Site NGHP-01-10.

The multi-channel seismic data show the presence of a BSR (Fig. 1b). The core is located on top of a mound presumably related to neo/shale tectonic activity. The fault system formed due to these activities facilitated the upward movement of fluid/gas leading to gas hydrate accumulation and cold seep formation (Dewangan et al., 2010; Reidel et al., 2010). Several mud diapirs, gas charged sediments, pockmarks, and other geological and geophysical proxies indicating the subsurface presence of gas are reported in the study area (Ramana et al., 2009). The analysis of sub-bottom profiler data (Mazumdar et al., 2009; Mazumdar et al., 2012a) suggests the presence of layered sediment as well as mass-transport deposits (MTD).

Sedimentological analysis of the core reveals hard authigenic carbonates of variable morphological types between 15 and 20 mbsf (Mazumdar et al., 2009). The porosity drops sharply to 25-50 % within this zone from a background porosity of about 75% and the carbonate content increases up to 20-60 vol %. Numerous well preserved and fragmented shells of chemosynthetic clam *Callyptogena* sp. were recorded within this zone suggesting a paleo-cold seep event. The AMS ¹⁴C dates (cf., Mazumdar et al., 2009; Fig. 8) show a variable sedimentation rate; the upper 3 m of sediment layers shows a high sedimentation rate of 248.3 cm/ kyr which drops to 86.7 cm/ kyr between 3 and 7 mbsf. Below 7 m, sedimentation rate abruptly drops to 17.5 cm/kyr and remains constant till 13 mbsf.

3. Methodology

The core was cut at one meter intervals and sub-sampling for gas and pore-water was carried out within one and a half hour after the core retrieval. The remaining core sections were kept for six to eight hours to equilibrate the temperature of the core sections to that of the surrounding. The wet-bulk density and magnetic susceptibility of the whole core was measured using onboard GeoTek multi-sensor core logger (MSCL) following standard calibration and measurement protocols. The core sections were longitudinally split into halves; one half was used for further sampling while the other half was kept as archive. Sub-sampling of the working half was carried out using 1 inch cylindrical sample bottles for magnetic measurements. After obtaining the natural remanent magnetism (NRM) data using Molspin spinner magnetometer, samples were oven dried at a temperature of about 40°C (with the bottle caps open) for nearly six days. Dried samples were crushed to disturb the orientation of the sample and were repacked in a clean wrap. The weight of each sample without the weight of the bottle and clean wrap

was recorded for normalization. Low frequency mass magnetic susceptibility (χ) was measured using Agico multifunction frequency kappabridge at a central frequency of 976 Hz; the same instrument was used to measure high frequency magnetic susceptibility (χ_{hf}) at a central frequency of 15616 Hz. Frequency-dependent magnetic susceptibility [$\chi_{fd}(\%)$] was computed using the formula,

$$\chi_{fd}(\%) = (\chi - \chi_{hf})/\chi \times 100. \quad (\text{Eq. 1})$$

Anhyseretic remanent magnetization (ARM) was imparted to each sample using an AF demagnetizer by applying a constant field of 100 mT with a 0.05 mT DC bias. The remanent magnetization was measured using Molspin spinner magnetometer. In a similar fashion, saturation isothermal remanent magnetization (SIRM) was imparted to the sample by applying a constant field of 1T in the forward direction using Molspin 1T pulse magnetizer, and its remanent magnetism was measured. Isothermal remanent magnetization (IRM) measurements were subsequently obtained at backward fields of -20 mT, -30 mT, -100 mT and -300 mT. The mineral magnetic parameter S-ratio is computed from the ratio of backfield IRM_{0.3T} and SIRM (Thompson and Oldfield, 1986).

The temperature-susceptibility measurements of each selected sample were obtained using Bartington (χ -T) system. The hysteresis loops for the selected samples were measured using a vibrating sample magnetometer (VSM). The magnetic particles were extracted from the slurry of sediment by dripping it over a gently inclined u-shaped elongated aluminum plate placed over a strong permanent magnet (1 T). The magnetic particles were retained in the plate while the non-magnetic slurry was collected into a dish placed at the lower end of the plate. A SEM (JEOL JSM-5800LV) was used to capture the images of the magnetic extract while its elemental analysis was carried out using an energy dispersive X-ray spectroscopy (EDS). Magnetic mineralogical identification of some selected samples was also carried out using Philips diffractometer (PW1840). All the samples were run from 15° to 70° 2theta at 3°/min scan speed using CuK α radiation ($\lambda = 1.541838\text{\AA}$).

4. Results

4.1 Analysis of environmental magnetic parameters

The environmental magnetic parameters such as χ , SIRM, ARM, soft-IRM, hard-IRM and S-ratio, and wet-bulk density of the sediment core are shown in Figure 2. The magnetic granulometry parameters ARM/SIRM, frequency-dependent magnetic susceptibility [$\chi_{fd}(\%)$], SIRM/ χ and low-frequency mass specific magnetic susceptibility measured in the laboratory along with volume-based

magnetic susceptibility measured onboard R/V *Marion Dufresne* are shown in Figure 3. We have broadly classified the magnetic profiles into two major zones based on the concentration, composition and granulometry data (Figs. 2 and 3). The depth ranges of major zones are 0-8.22 mbsf for *zone 1* and 8.22-30 mbsf for *zone 2*. In *zone 1*, SIRM, ARM, soft-IRM and hard-IRM show a gradual decrease with depth, while the S-ratio remains close to unity. The ARM/SIRM ratio shows a linear increase up to 7.5 mbsf and thereafter it abruptly decreases towards the bottom of *zone 1*. $\chi_{fd}(\%)$ shows an overall increase up to 5 mbsf and decreases towards the end of *zone 1*, while the SIRM/ χ ratio shows a linear decrease up to 5 mbsf and then increases to the end of *zone 1*.

The beginning of *zone 2* is marked by an abrupt decrease of magnitudes of χ , SIRM, ARM and soft-IRM. The hard-IRM shows a marginal linear decrease within *zone 2*. This zone will be referred to as the zone of reduced magnetic susceptibility in the subsequent paragraphs. The S-ratio abruptly decreases in the beginning of *zone 2* and thereafter it increases towards unity with depth. The grain size dependent parameters ARM/SIRM and SIRM/ χ also show an abrupt decrease at the start of *zone 2*. Within *zone 2*, we observed a zone of enhanced susceptibility from 17.68-23.6 mbsf which will be referred to as *zone 2a*. This zone is characterized by an abrupt increase in $\chi_{fd}(\%)$ values from 2 to 12 with an average value of 8. An increase in the values of χ , SIRM, ARM and soft-IRM is also observed in *zone 2a*. The values of hard-IRM and S-ratio are almost close to zero and unity, respectively. The lab-based magnetic susceptibility which was measured one year later shows a marked decrease when compared to shipboard susceptibility measurements within this zone. The parameters SIRM/ χ and ARM/SIRM do not show any anomalous behavior in this zone.

4.2 Thermomagnetic and hysteresis curves of selected samples

The dependence of susceptibility with temperature during heating and cooling of selected samples within *zone 1* at different depths is shown in Fig. 4a-d. Temperature profiles during heating are different from those obtained while cooling. During heating, the susceptibility increases up to a temperature of 325-350 °C and thereafter it decreases with temperature. The cooling curves show comparatively lower variations in susceptibility with temperature.

The selected samples in *zone 2* at different depths (Fig. 4e, h) show almost constant susceptibility values up to 400 °C. The susceptibility increases sharply to the maximum value at 505 °C and thereafter it reduces to a minimum value at 600 °C. The samples in *zone 2a* (Fig. 4f, g) show a drop in magnetic susceptibility up to 330 °C and thereafter it increases to a maximum value at around 520 °C

and further increase in temperature leads to a drop in magnetic susceptibility. The cooling curves show higher magnetic susceptibility at low temperatures as compared to those of heating curves.

The hysteresis loops of the selected samples are shown in Figure 5. The coercive force (H_c) derived from the hysteresis loop in *zone 1* (Fig. 5a-d) decreases from 8.24 mT at 0.52 mbsf to 7.81 mT at 3.84 mbsf. The coercive force again increases to 8.12 mT at 5.6 mbsf and then reduces to 7.23 mT at 7.94 mbsf. At 9.78 mbsf in *zone 2*, the sigmoidal shaped hysteresis loop (Fig. 5e) is closed with reduced value of saturation remanence and the coercive force is close to 11.44 mT. The hysteresis loops in *zone 2a* (Fig. 5f, g) show similar behavior with a lower coercive force close to 6 mT.

4.3 SEM-EDS analyses of magnetic minerals

The SEM images of the magnetic minerals at different depths are shown in Fig. 6. At shallow depth (6.8 mbsf) in *zone 1*, dissolution of small titanomagnetite grains ($< 2 \mu\text{m}$) is observed. The octahedral titanomagnetite grain (marked in Fig. 6a) is dissolved leading to a complicated honeycomb structure. Several dissolution pits are observed on the surface of other titanomagnetite grains. The EDS results of the titanomagnetite grains show the presence of iron and titanium with traces of aluminum, manganese, vanadium and magnesium. The Ti/Fe ratio of these grains ranges from 0.2 to 0.45. At deeper depth (10 mbsf) in *zone 2*, most of the small magnetic grains are dissolved and the larger ones ($> 10 \mu\text{m}$) show signs of dissolution particularly at the corners of the crystals (Fig. 6b). The dissolution of titanohaematite crystals (Fig. 6c) at 11.16 mbsf, results in a complex assemblage of quadrangle plate like structures. The EDS results of titanohaematite grains show the presence of iron and titanium with traces of aluminum and magnesium. The Ti/Fe ratio of such grains ranges from 0.8 to unity. A large titanohaematite grain (~ 15.22 mbsf) in *zone 2* also show complex dissolution pattern (Fig. 6d).

In the zone of reduced magnetic susceptibility (*zone 2*), numerous framboidal pyrite crystals are observed in the magnetic extract (Fig. 7a), with negligible fillings. The EDS results show the presence of iron and sulfur with the S/Fe ratio close to two. The sizes of individual framboids vary between 5 and 25 μm . In *zone 2a*, the pyrite framboids (Fig. 7b) are filled with fine grain material. The zoom outs of the framboids (Fig. 7c, d) show individual pyrite crystal surrounded by fine grained amorphous material. The EDS results of large pyrite grains and filling material show the presence of iron and sulfur with the S/Fe ratios close to two and slightly larger than unity, respectively. The iron-sulfide fillings surrounding the pyrite crystals appear to be due to a diagenetic process as they exhibit different morphology and composition than those of pyrite crystals.

4.4 XRD analysis of magnetic minerals

The X-ray diffraction (XRD) curve (Fig. 8a) of the magnetic minerals at shallow depth (0.54 mbsf) shows the peaks corresponding to titanomagnetite and quartz. The XRD peaks in the zone of reduced magnetic susceptibility (*zone 2*) confirm the presence of pyrite (Fig. 8b). The XRD peaks in *zone 2a* show a mixture of pyrite and greigite (Fig. 8c).

4.5 Low temperature remanence measurements in zone 2a

The samples from *zone 2a* were analyzed for the identification of magnetic minerals using low-temperature remanence measurements at the Institute of Rock Magnetism (IRM), Minnesota, USA. The thermal demagnetization of a 2.5T IRM (imparted at 10° K; ZFC) and the low-temperature cycling of a 2.5T IRM (imparted at room temperature; RTSIRM) were acquired (Fig. 9). Low-temperature SIRM warming curves are used to differentiate greigite from other magnetic minerals such as magnetite and pyrrhotite (Fe₇S₈) based on low-temperature magnetic transitions (Moskowitz et al., 1993; Roberts, 1995; Housen and Musgrave, 1996; Roberts et al., 1996; Torii et al., 1996; Horng et al., 1998). The low temperature SIRM (Fig. 9a-c) rapidly decreases upon warming to less than 10% of its initial value at room temperature indicating substantial paramagnetic behavior. The data show no evidence of pyrrhotite, since magnetic change associated with the 34 ° K transition is negligible; however, the nanoparticles of pyrrhotite may remain undetected by this method (Worm et al., 1993). The low temperature cycling of RTSIRM (Fig. 9d-f) shows that the SIRM increases rapidly as the temperature decreases, and the warming and cooling curves are different at 120 ° K (Verwey transition) indicating the presence of magnetite.

$\chi(T,f)$ curves (where T and f are the temperature and frequency, respectively) for a selected sample at 21.36 mbsf (*zone 2a*) is shown in Fig. 10. The low-temperature susceptibility data show a strong paramagnetic background and the real $\chi'(T,f)$ and imaginary $\chi''(T,f)$ components show frequency dependent properties indicating the presence of superparamagnetic domain ferrimagnetic particles. A blocking temperature (T_B) is observed in the χ'' curve (Fig. 10b) below 20 ° K. Another T_B can be inferred around 100-110 ° K where reversal in frequency behavior is observed (low frequency measurements are higher than those of high frequency for temperatures less than 100 ° K and vice-versa).

5. Discussion

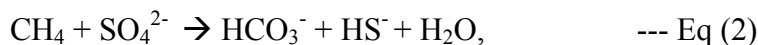
5.1 Alteration of magnetic minerals due to sulfate reduction

The present day sulfate profile (reproduced from Mazumdar et al., 2009) can be divided into three segments (I-III) with gradients 0.032 mM/cm, 0.0038 mM/cm and 0.034 mM/cm (Fig. 11b). The S-shaped sulfate concentration profile is attributed to the combined effect of rapid sedimentation (segment I) and anaerobic methane oxidation (AOM, segment III). The kink type profiles suggest transient or non-steady state pore water chemistry (Hensen et al., 2003; Henkel et al., 2011). The change in gradient of sulfate concentration profile below 3 m (segment II) may be correlated with the abrupt decrease in sedimentation rate from 248.3 to 86.7 cm/kyr. Under oxic bottom water conditions, sedimentation rate plays an important role in determining the preservation and the pathway of organic matter decomposition and its availability to sulfate reducers (Canfield, 1991, 1994; Tyson, 1995). Based on $\delta^{13}\text{C}_{\text{TOC}}$ of KG basin sediments (-14 to -22 ‰ VPDB, Mazumdar et al., 2011) and headspace $\delta^{13}\text{C}_{\text{CO}_2}$, Mazumdar et al (2012a) suggested primarily organo-clastic sulfate reduction for the upper 3-4 m of sediment at MD161/8 as compared to the dominance of AOM driven sulfate reduction within 16-18 mbsf. The approximate depth of sulfate-methane transition zone (SMTZ) is highlighted by a double arrow (from 13 to 17 mbsf) in figure 11b. In the continental margin off Uruguay and lower Zaire (Congo) deep sea, the kink and overall concave up character of sulfate profiles recorded from fan have been attributed to overthrusting of sediment (decoulement) by cohesive slide block (Zabel and Schulz, 2001; Hensen et al., 2003). However, the continuous ^{14}C ages for the top 5 m at MD161/8 do not indicate mass-flow related processes (Mazumdar et al., 2009; Mazumdar et al., 2012a). High sedimentation rate without any pronounced discontinuity has also been reported at other locations in KG offshore basin. The nonzero sulfate concentration below 17 mbsf is attributed to either pyrite oxidation (Bottrel et al., 2000) or incomplete sulfate reduction owing to transient state and relatively recent upward migration of methane (Ussler and Paull, 2008).

In general, organo-clastic sulfate reduction accounts for the bulk of the organic matter mineralization in marine sediments through anaerobic pathways and can be represented as (e.g., Herlihy et al., 1987),



Another process governing the sulfate reduction is AOM, which is attributed to a consortium of CH₄-oxidizing archaea and sulfate-reducing bacteria (Hoehler et al. 1994; Borowski et al., 1996; Hinrichs et al., 1999; Boetius et al., 2000) and can be represented as,



The HS⁻, which is produced via the organo-clastic/AOM sulfate reduction pathways (eqs. 1 and 2), reacts with the magnetic minerals leading to their reductive dissolution (Berner, 1970; Poulton et al., 2004),



The dissolved Fe²⁺ further reacts with HS⁻ to form iron monosulfide (FeS),



Although the exact mechanism of pyrite formation is unknown, Sweeney and Kaplan (1973) proposed a mechanism for conversion of iron monosulfide to pyrite with greigite being an intermediate product and can be represented by eq. 6,



Alternately, Hunger and Benning (2007) has proposed a mechanism for the conversion of FeS to FeS₂ represented by the equation,



These above geochemical processes are primarily responsible for the dissolution of magnetic minerals in marine sediments. The SEM-EDS and the XRD analyses of magnetic extracts (Fig. 8) suggest that titanomagnetite with varying Ti/Fe ratios (0.2 to 0.45) is the primary magnetic mineral. Curie temperatures of 350-580°C derived from the thermomagnetic curves of the sediment samples (Fig. 4a-d) further confirm that the titanomagnetite is the primary magnetic mineral. The linear increase in the ARM/SIRM ratio (Fig. 3a) for the upper 7 m of sediment column suggests a relative increase in the concentration of stable single domain particles (cf. Maher, 1988). Likewise, the decrease in the SIRM/χ ratio (Fig. 3c) indicates a relative decrease in the abundance of finer magnetic particles (Thomsen and Oldfield, 1986). These observations show reductive dissolution of magnetic minerals with finer particles dissolving faster than coarser particles (Karlin and Levi, 1983). The SEM images of the magnetic extract

at a depth of 6.8 mbsf (Fig. 6a) show the characteristic features of dissolution i.e., itch and pit signatures thereby confirming the dissolution of primary magnetic minerals. However, the parameter $\chi_{fd}(\%)$, which is sensitive to superparamagnetic (SP) particles, shows a slight increase within 0-5 mbsf (Fig. 3b). Such enhancement of ultra-fine grains exhibiting SP behavior was initially observed by Tarduno (1995), and later explained by Rowan and Robert (2006) that such enhancement is due to the presence of authigenic greigite. Further downcore (7-8.22 mbsf), the systematic decrease in the ARM/SIRM ratio suggests the dissolution of stable single domain particles which is due to the reaction of magnetic minerals with sulfide. The coarser euhedral grains of titanomagnetite (Fig. 6b) and a plate-shaped titanohaematite grain (Fig. 6c) in *zone 2* also show sign of dissolution particularly at the corners.

5.2 Zone of reduced susceptibility due to AOM (zone 2)

A zone of reduced magnetic susceptibility is observed below 8.22 mbsf (*zone 2*). This zone is characterized by lower values of magnetic susceptibility, ARM, SIRM, and soft-IRM indicating low concentration of magnetic minerals. The XRD analysis (Fig. 8b) and SEM images (Fig. 7a) of magnetic minerals from this zone confirm the presence of framboidal pyrite. The EDS analysis of the pyrite crystals shows the presence of iron and sulfur elements with S/Fe ratio close to two. The thermo magnetic curves (Fig. 4e-h) also suggest the presence of pyrite as inferred from the oxidation cycle of pyrite to magnetite, maghemite and finally to hematite resulting in the increase in magnetization above 450°C and subsequent decrease with temperature (Roberts and Pillans, 1993; Passier et al., 2001; Tudryn and Tucholka, 2004).

The chromium reducible sulfur (CRS) concentration profile (Fig. 11c; Peketi et al., 2012) represents the pyritization within the sediment column. The sharp decrease in susceptibility within *zone 1* (5 – 8.22 mbsf) is inversely correlatable to comparable increase in CRS concentration. It is interesting to note that the CRS concentration in *zone 2* (~0.5 to 3.7 wt %) is higher than that observed in *zone 1* (0.04 to 0.41 wt %). The CRS concentration in the sediments depends on the availability of reactive iron and hydrogen sulfide during early/late diagenesis. Dominance of AOM activity within the paleo-SMTZ (Peketi et al., 2012) is evident from the occurrence of ^{12}C enriched authigenic carbonates.

Detailed sedimentological study in the zone of reduced magnetic susceptibility shows the presence of authigenic carbonates (Table 2 in Mazumdar et al., 2009) whose locations are plotted along with the magnetic susceptibility (Fig. 11a). These carbonates show highly depleted carbon isotopic composition ($\delta^{13}\text{C}$ ranging from -41.3 to -52.4 ‰ VPDB) typically reported for methane derived

authigenic carbonates (Mazumdar et al., 2009). The presence of chemosynthetic clams like *Callyptogena* are observed in the zone of enhanced carbonate precipitation (between 16 and 18 mbsf) suggesting paleo-seepage of methane and sulfidic rich fluid at the studied site. The geochemical signatures such as increase in CRS concentration, presence of methane derived authigenic carbonates, and depleted $\delta^{13}\text{C}_{\text{TIC}}$ in the zone of reduced susceptibility suggest that the abrupt drop in the values of magnetic susceptibility, SIRM, and ARM is due to the reductive dissolution of magnetic minerals by HS^- (eqs 3 and 4) which is released during the process of sulfate reduction via AOM (eqs 3-7). The paleo-depth of SMTZ governs the dissolution of magnetic minerals in the zone of reduced susceptibility. Such dissolution of magnetic minerals due to AOM is well documented in literature (Kasten et al., 1998; Jørgensen et al., 2004; Neretin et al., 2004; Riedinger et al., 2005; Garming et al., 2005; Novosel et al., 2005; Horng and Chen, 2006). The S-ratio, which indicates the relative abundance of magnetite and hematite, decreases abruptly from unity to 0.5 at the beginning of *zone 2* suggesting larger abundance of hematite and further it increases gradually towards unity with depth. This observation suggests that hematite is less prone to dissolution compared to magnetite. Similar observation has been reported in the continental shelf sediments from the Korea Strait (Liu et al., 2004).

No visible precipitate was observed when the pore-water samples were treated with Cd during preliminary sulfide measurements of core NGHP-01-10 onboard JOIDES Resolution (A. Spivack, personal communication; Collett et al., 2008). In the absence of detectable sulfide concentration in the sediment pore water within the present SMTZ, the contribution of modern pyritization is difficult to assess

5.3 Zone of marked greigite enrichment (zone 2a)

A zone of enhanced susceptibility (*zone 2a*) within *zone 2* is observed. It is likely that most of the primary magnetic minerals are dissolved in *zone 2a* due to reductive dissolution. Therefore, we presume that the larger values of magnetic susceptibility are due to the presence of authigenic magnetic minerals. Greigite (Fe_3S_4) and pyrrhotite (Fe_7S_8) are the main ferrimagnetic minerals formed as an intermediate to pyrite during the pyritization processes (Snowball and Thomsen, 1990; Robert, 1995; Rowan and Robert, 2006). Low-temperature measurements of selected samples in *zone 2a* show the absence of pyrrhotite as the magnetic change associated with the 34°K transition is not observed (Fig. 9). Therefore, it is likely that the authigenic magnetic mineral is greigite. The XRD (Fig. 8c) and SEM-EDS analyses of the magnetic minerals confirm the presence of greigite. The lower values of lab-based

mass-magnetic susceptibility as compared to the onboard volume-magnetic susceptibility (Fig. 3d) indicate reduction in magnetic susceptibility during storage of sediment samples. Such reduction in magnetic susceptibility with time is another indication for the presence of greigite as the magnetic intensity of the greigite bearing horizon is known to decrease with time due to the oxidation (Hilton, 1990). *Zone 2a* is characterized by an abrupt increase in χ_{rd} (%) from 2 to 12 (Fig. 3b) suggesting the presence of superparamagnetic (SP) grain size particles. A blocking temperature (T_B) below 20°K in the χ'' curve (Fig. 10b) is also related to SP greigite. A similar blocking temperature below 20°K was observed for synthetic greigite sample and may be related to oxidation of greigite particles (Chang, et al., 2009). During reductive dissolution (eqs 3 and 4), the SP particles are likely to dissolve faster than the coarser particles (Karlin and Levi, 1983). Therefore, the observed increase in the abundance of SP particles suggests the presence of authigenic greigite (cf. Rowan and Robert, 2006). The SEM images of the magnetic minerals show the presence of framboidal pyrite grains that are filled with fine grained particles (Fig. 6b-d). The EDS analysis confirms that the framboidal grains are pyrite while the fine grained particles are greigite. We propose that the pyrite crystals are formed due to pyritization process related to AOM and the formation of fine grained greigite over the existing pyrite crystal appears to be due to diagenetic process. Similar occurrence of SP/SD grain sized greigite has been reported from different geological environments (Jiang et al., 2001; Jørgensen et al., 2004; Neretin et al., 2004; Liu et al., 2004; Roberts and Weaver, 2005; Horng and Chen, 2006; Rowan and Robert, 2006; Fu et al., 2008; Rowan et al., 2009).

5.4 Possible mechanisms for greigite formation in KG offshore basin

In marine environment, relative rates of HS^- production and the availability of reactive iron controls the pyritization process (Wilkins and Barnes, 1997). In case of excess HS^- and high availability of reactive iron, the pyritization process is complete and the metastable iron sulfides are eventually converted to pyrite (Berner, 1967; Mazumdar et al., 2012b). However, insufficient supply of HS^- leads to partial pyritization. Under low HS^- concentration greigite may preferentially be precipitated over pyrite and will lead to the preservation of greigite in marine sediment.

If we consider the present day sulfate profile (Fig. 11b), *zone 2a* lies below the current depth of SMTZ and is attributed to the presence of SP/SD greigite. Greigite being a ferrimagnetic mineral can record the paleomagnetic signal at the time of its formation leading to contradictory polarities within the same stratigraphic horizon (Horng et al., 1998; Jiang et al., 2001; Roberts et al., 2005) or spurious

magnetic polarity patterns that are inconsistent with independent age controls (Florindo and Sagnotti, 1995; Rowan and Roberts, 2005; Sagnotti et al., 2005). Various mechanisms are proposed for the formation of authigenic greigite in marine sediments. One such mechanism is the downward diffusion of sulfide below the SMTZ which may lead to limited amounts of sulfide in the pore water (Rowan and Robert, 2006; Rowan et al., 2009). In such a scenario, SP/SD greigite would form close to the SMTZ and relative abundance of SD greigite increases down-core as observed in the Oman continental margin and northern California. It is possible that the sulfide released during AOM might be diffusing beyond the boundaries of the SMTZ. The diffusion process can lead to limited sulfide outside the SMTZ which will arrest the pyritization process and favor the preservation of authigenic greigite below the SMTZ (Rowan et al., 2009). The presence of a thick authigenic carbonate layer beneath the SMTZ (Mazumdar et al., 2009) might have hindered the downward diffusion of sulfide favoring early arrest of the pyritization process and preservation of SP/SD greigite. However, the negligible sulfide concentration at Site NGHP-01-10 indicates that sulfide is immediately converted to mackinawite upon formation. Hence, it is unlikely that the mechanism involving downward diffusion of sulfide from current depth of SMTZ can explain the greigite formation in *zone 2a*.

Peketi et al. (2012) showed a marked enrichment of H₂S in the sediment ~60 kyr ago which led to H₂S diffusion across sediment water interface. We propose that the downward diffusion of HS⁻ from the upper high concentration zone might have led to greigite precipitation in *zone 2a* during intense AOM in the past. The presence of isotopically depleted carbonates from 8 to 30 mbsf also suggests the paleo-intensification of AOM. Such intensification of AOM can be linked to the waxing and waning of the methane flux which may be related to the opening and closing of the fault system formed due to neo/shale tectonism (Dewangan et al., 2010; Mazumdar et al., 2012a). The temporal variations in methane flux are reported to be closely linked to the deeper gas hydrate deposits and are studied based on the geochemical indicators such as authigenic barite formation, calcium carbonate precipitation and records of pyrite concentration (Torres et al., 1996; Dickens, 2001; Teichert et al., 2003; Lim et al., 2011). The absence of Ba/Al enrichment peak in the studied cores indicates possible dissolution of barite due to upward movement of SMTZ, or a low Ba flux to the sediment (Peketi et al., 2012). We believe that this mechanism of greigite formation due to paleo-SMTZ might be applicable to the regions of variable methane flux related to the subsurface gas hydrate deposits.

An alternative model of greigite formation involves anaerobic oxidation of pyrite and subsequent reduction of the regenerated sulfate to HS⁻ (Bottrell et al., 2000; Jiang et al., 2001; Larrasoña et al.,

2007). Greigite enrichment indicates relatively low concentration of HS^- to that of reactive iron. Low concentration of HS^- may be attributed to either low concentration of sulfate and/or methane in deeper sediments. Record of nonzero sulfate concentration observed below 17 mbsf at MD161/8 may also be possibly linked to the greigite formation in KG offshore basin. In order to resolve which mechanism is responsible for greigite formation and preservation in KG offshore basin, additional geochemical investigations are required.

6. Conclusions

The diagenesis of the magnetic mineral assemblages is studied in a sediment core located in the gas hydrate/cold seep region in the KG offshore basin. The dominant magnetic mineral is titanomagnetite with trace amount of titanohematite. These magnetic minerals are dissolved due to the HS^- released during anaerobic oxidation of methane (AOM). The dissolution is evident in magnetic profile as a zone of reduced magnetic susceptibility. The thermomagnetic curves, SEM images, EDS and XRD analyses, and available geochemical data suggest the presence of framboidal pyrite in this zone.

A zone of enhanced susceptibility (*zone 2a*) is observed, where the presence of SP/SD sized greigite is confirmed by the SEM-EDS and XRD analyses. Greigite zone occurs below the current depth of SMTZ. The occurrence of greigite in the interstices between the pyrite crystals suggests that it is formed after framboidal pyrite. Our data show that in gas hydrate/cold seep settings the location of the SMTZ is prone to sudden shifts due to the variability in methane flux. Fluctuation in the SMTZ on short time scales do not allow any accumulation of sulfide and thus can lead to the formation of greigite. Alternatively, anaerobic oxidation of pyrite and subsequent reduction of the regenerated sulfate to HS^- can lead to greigite formation. The authigenic formation of this mineral and subsequent alteration of the primary magnetic signal not only has strong implications for the interpretation of paleomagnetic records, but also might be a useful indicator for the location of paleo-SMTZ. It might also help to understand the accumulation and dissociation of gas hydrates in paleo environments. However further investigations are required to understand the formation and preservation of greigite.

Acknowledgements

We thank the directors of NIO, IIG, NIOT, NCAOR and advisor MOES for supporting this study. Head, oceanography department, and in-charge, on-board operations of IPEV are thanked for providing onboard technical support and facilities. Sincere thanks to students of Goa University, IIT Kharagpur

and project scientists of NIO, NIOT, PRL and NGRI. We thank Dr. Mike Jackson, Institute for Rock Magnetism (IRM), university of Minnesota, USA for carrying out low temperature measurements of selected samples. We would like to thank Dr. S. Kasten and an anonymous reviewer for their comments which have improved the quality of the manuscript. This is CSIR-NIO contribution no. ----.

References

Berner, R.A., 1967. Thermodynamic stability of sedimentary iron sulfides. *American Journal of Science* 265(9), 773-785.

Berner, R.A., 1970. Sedimentary pyrite formation. *American Journal of Science* 268(1), 1-23.

Berner, R.A., 1984. Sedimentary pyrite formation: an update. *Geochimica et Cosmochimica Acta* 48(4), 605-615.

Boetius, A., Ravenschlag, K., Schubert, C.J., Rickert, D., Widdel, F., Gieseke, A., Amann, R., Jørgensen, B.B., Witte, U., Pfannkuche, O., 2000. A marine microbial consortium apparently mediating anaerobic oxidation of methane. *Nature* 407(6804), 623- 626.

Borowski, W.S., Paull, C.K., Ussler III, W., 1996. Marine pore-water sulfate profiles indicate in situ methane flux from underlying gas hydrate. *Geology* 24(7), 655-658.

Bottrell, S.H., Parkes, R.J., Cragg, B.A., Raiswell, R., 2000. Isotopic evidence for anoxic pyrite oxidation and stimulation of bacterial sulphate reduction in marine sediments. *Journal of the Geological Society* 157(4), 711-714.

Canfield, D.E., Berner, R.A., 1987. Dissolution and pyritization of magnetite in anoxic marine sediments. *Geochimica et Cosmochimica Acta* 51(3), 645-659.

Canfield, D. E., 1991. Sulfate reduction in deep-sea sediments. *American Journal of Science* 291(2), 177-188.

Canfield, D. E., 1994. Factors influencing organic carbon preservation in marine sediments. *Chemical Geology* 114(3-4), 315 -329.

Chang, L., Roberts, A.P., Rowan, C.J., Tang, Y., Pruner, P., Chen, Q., Horng, C. S., 2009. Low-temperature magnetic properties of greigite (Fe₃S₄). *Geochemistry Geophysics Geosystems* 10(1), Q01Y04. doi: 10.1029/2008GC002276.

Collett, T., Reidel, M., Cochran, J., Boswell, R., Presley, J., Kumar, P., Sathe, A., Sethi, A., Lall, M., Sibal, V., NGHP Expedition 01 scientists., 2008. Results of the Indian National Gas Hydrate Program Expedition 01 initial reports, Dir. Gen. of Hydrocarbons, Min. of Pet. and Nat. Gas, New Delhi.

Dickens, G.R., 2001. Sulfate profiles and barium fronts in sediment on the Blake Ridge: present and past methane fluxes through a large gas hydrate reservoir. *Geochimica et Cosmochimica Acta* 65(4), 529-543.

- Dewangan, P., Ramprasad, T., Ramana, M.V., Mazumdar, A., Desa, M., Badesab, F. K., 2010. Seabed morphology and gas venting features in the continental slope region of Krishna-Godavari basin, Bay of Bengal: implications in gas-hydrate exploration. *Marine and Petroleum Geology* 27(7), 1628-1641.
- Florindo, F., Sagnotti, L., 1995. Palaeomagnetism and rock magnetism in the upper Pliocene Valle Ricca (Rome, Italy) section. *Geophysical Journal International* 123(2), 340-354.
- Froelich, P.N., Klinkhammer, G.P., Bender, M.L., Luedtke, N.A., Heath, G.R., Cullen, D., Dauphin, P., Hammond, D., Hartman, B., Maynard, V., 1979. Early oxidation of organic matter in pelagic sediments of the eastern equatorial Atlantic: suboxic diagenesis. *Geochimica et Cosmochimica Acta* 43(7), 1075-1090.
- Fu, Y., von Dobeneck, T., Franke, C., Heslop, D., Kasten, S., 2008. Rock magnetic identification and geochemical process models of greigite formation in Quaternary marine sediments from the Gulf of Mexico (IODP Hole U1319A). *Earth and Planetary Science Letters* 275(3-4), 233-245.
- Garming, J.F.L., Bleil, U., Riedinger, N., 2005. Alteration of magnetic mineralogy at the sulfate--methane transition: analysis of sediments from the Argentine continental slope. *Physics of the Earth and Planetary Interiors* 151(3-4), 290-308.
- Gibbs, R.J., 1977. Clay mineral segregation in the marine environment. *Journal of Sedimentary Petrology* 47(1), 237-243.
- Henkel, S., Strasser, M., Schwenk, T., Hanebuth, T.J.J., Hüsener, J., Arnold, G.L., Winkelmann, D., Formolo, M., Tomasini, J., Krastel, S., Kasten, S., 2011. An interdisciplinary investigation of a recent submarine mass transport deposit at the continental margin off Uruguay. *Geochemistry Geophysics Geosystems* 12(8), Q08009. doi: 10.1029/2011GC003669.
- Hensen, C., Zabel, M., Pfeifer, K., Schwenk, T., Kasten, S., Riedinger, N., Schulz, H.D., Boetius, A., 2003. Control of sulfate pore-water profiles by sedimentary events and the significance of anaerobic oxidation of methane for the burial of sulfur in marine sediments. *Geochimica et Cosmochimica Acta* 67(14), 2631-2647.
- Herlihy, A.T., Mills, A.L., Hornberger, G.M., Bruckner, A.E., 1987. The importance of sediment sulfate reduction to the sulfate budget of an impoundment receiving acid mine drainage. *Water Resources Research* 23, 287-292.
- Hilton, J., 1990. Greigite and the magnetic properties of sediments. *Limnology and Oceanography* 35, 509-520.
- Hinrichs, K.U., Hayes, J.M., Sylva, S.P., Brewer, P.G., DeLong, E.F., 1999. Methane-consuming archaeobacteria in marine sediments. *Nature* 398(6730), 802-805.
- Hoehler, T.M., Alperin, M.J., Albert, D.B., Martens, C.S., 1994. Field and laboratory studies of methane oxidation in an anoxic marine sediment Evidence for a methanogen-sulfate reducer consortium. *Global Biogeochemical Cycles* 8(4), 451-463.

- Horng, C.S., Torii, M., Shea, K.S., Kao, S.J., 1998. Inconsistent magnetic polarities between greigite- and pyrrhotite/magnetite-bearing marine sediments from the Tsailiao-chi section, southwestern Taiwan. *Earth and Planetary Science Letters* 164(3-4), 467-481.
- Horng, C.S., Chen, K.H., 2006. Complicated magnetic mineral assemblages in marine sediments offshore of southwestern Taiwan: possible influence of methane flux on the early diagenetic process. *Terrestrial Atmospheric and Oceanic Sciences* 17(4), 1009-1026.
- Housen, B. A., Musgrave, R.J., 1996. Rock-magnetic signature of gas hydrates in accretionary prism sediments. *Earth and Planetary Science Letters* 139(3-4), 509-519.
- Hunger, S., Benning, L.G., 2007. Greigite: a true intermediate on the polysulfide pathway to pyrite. *Geochemical Transactions* 8(1). doi: 10.1186/1467-4866-8-1.
- Jiang, W.T., Horng, C.S., Roberts, A.P., Peacor, D.R., 2001. Contradictory magnetic polarities in sediments and variable timing of neof ormation of authigenic greigite. *Earth and Planetary Science Letters* 193(1-2), 1-12.
- Jørgensen, B.B., Böttcher, M.E., Lüschen, H., Neretin, L.N., Volkov, I.I., 2004. Anaerobic methane oxidation and a deep H₂S sink generate isotopically heavy sulfides in Black Sea sediments. *Geochimica et Cosmochimica Acta* 68(9), 2095-2118.
- Kao, S.J., Horng, C.S., Roberts, A.P., Liu, K.K., 2004. Carbon-sulfur-iron relationships in sedimentary rocks from southwestern Taiwan: influence of geochemical environment on greigite and pyrrhotite formation. *Chemical Geology* 203(1-2), 153-168.
- Karlin, R., Levi, S., 1983. Diagenesis of magnetic minerals in recent hemipelagic sediments. *Nature* 303(5915), 327-330.
- Karlin, R., Levi, S., 1985. Geochemical and sedimentological control of the magnetic properties of hemipelagic sediments. *Journal of Geophysical Research* 90(B12), 10373-10392.
- Karlin, R., Lyle, M., Heath, G.R., 1987. Authigenic magnetite formation in suboxic marine sediments. *Nature* 326(6112), 490-493. doi: 10.1038/326490a0.
- Karlin, R., 1990. Magnetite diagenesis in marine sediments from the Oregon continental margin. *Journal of Geophysical Research* 95(B4), 4405-4419.
- Kasten, S., Freudenthal, T., Gingele, F.X., Schulz, H.D., 1998. Simultaneous formation of iron-rich layers at different redox boundaries in sediments of the Amazon deep-sea fan. *Geochimica et Cosmochimica Acta* 62(13), 2253-2264.
- Larrasoaña, J.C., Roberts, A.P., Hayes, A., Wehausen, R., Rohling, E.J., 2006. Detecting missing beats in the Mediterranean climate rhythm from magnetic identification of oxidized sapropels (Ocean Drilling Program Leg 160). *Physics of the Earth and Planetary Interiors* 156(3-4), 283-293.
- Larrasoaña, J.C., Roberts, A.P., Musgrave, R.J., Gràcia, E., Piñero, E., Vega, M., Martínez-Ruiz, F., 2007. Diagenetic formation of greigite and pyrrhotite in gas hydrate marine sedimentary systems. *Earth and Planetary Science Letters* 261(3-4), 350-366.

- Lee, M.W., Collett, T.S., 2009. Gas hydrate saturations estimated from fractured reservoir at site NGHP-01-10, Krishna-Godavari basin, India. *Journal of Geophysical Research* 114(B7), B07102. doi: 10.1029/2008JB006237.
- Leslie, B.W., Hammond, D.E, Berelson, W.M., Lund, S.P., 1990. Diagenesis in anoxic sediments from the California continental borderland and its influence on iron, sulfur, and magnetite behavior. *Journal of Geophysical Research* 95(B4), 4453-4470.
- Lim, Y.C., Lin, S., Yang, T.F., Chen, Y.G., Liu, C.S., 2011. Variations of methane induced pyrite formation in the accretionary wedge sediments offshore southwestern Taiwan. *Marine and Petroleum Geology* 28(10), 1829-1837.
- Liu, J., Zhu, R., Roberts, A.P., Li, S., Chang, J.H., 2004. High-resolution analysis of early diagenetic effects on magnetic minerals in post-middle-Holocene continental shelf sediments from the Korea Strait. *Journal of Geophysical Research* 109(B3), B03103. doi: 10.1029/2003JB002813.
- Lyle, M., 1983. The brown-green color transition in marine sediments: a marker of the Fe (III)-Fe (II) redox boundary. *Limnology and Oceanography* 28(5), 1026-1033.
- Maher, B.A., 1988. Magnetic properties of some synthetic sub-micron magnetites. *Geophysical Journal* 94(1), 83-96.
- Mazumdar, A., Dewangan, P., João, H.M., Peketi, A., Khosla, V.R., Kocherla, M., Badesab, F.K., Joshi, R.K., Roxanne, P., Ramamurty, P.B., Karisiddaiah, S.M., Patil, D.J., Dayal, A.M., Ramprasad, T., Hawkesworth, C.J., Avanzinelli, R., 2009. Evidence of paleo-cold seep activity from the Bay of Bengal, offshore India. *Geochemistry Geophysics Geosystems* 10(6), Q06005. doi: 10.1029/2008GC002337.
- Mazumdar, A., Joshi, R. K., Peketi, A., Kocherla, M., 2011. Occurrence of faecal pellet-filled simple and composite burrows in cold seep carbonates: a glimpse of a complex benthic ecosystem. *Marine Geology* 289(1-4), 117–121. doi: 10.1016/j.margeo.2011.09.003.
- Mazumdar, A., João, H.M., Peketi, A., Dewangan, P., Kocherla, M., Joshi, R.K., Ramprasad, T., 2012a. Geochemical and geological constraints on the composition of marine sediment pore fluid: possible link to gas hydrate deposits. *Marine and Petroleum Geology* 38(1), 35-52.
- Mazumdar, A., Peketi, A., João, H.M., Dewangan, P., Borole, D.V., Kocherla, M., 2012b. Sulfidization in a shallow coastal depositional setting: Diagenetic and palaeoclimatic implications. *Chemical Geology* 322-323, 68-78.
- Moskowitz, B.M., Frankel, R.B., Bazylinski, D.A., 1993. Rock magnetic criteria for the detection of biogenic magnetite. *Earth and Planetary Science Letters* 120(3-4), 283-300.
- Musgrave, R.J., Bangs, N.L., Larrasoana, J.C., Gràcia, E., Hollamby, J.A., Vega, M.E., 2006. Rise of the base of the gas hydrate zone since the last glacial recorded by rock magnetism. *Geology* 34(2), 117-120.
- Neretin, L.N., Böttcher, M.E., Jørgensen, B.B., Volkov, I.I., Lüschen, H., Hilgenfeldt, K., 2004. Pyritization processes and greigite formation in the advancing sulfidization front in the Upper Pleistocene sediments of the Black Sea. *Geochimica et Cosmochimica Acta* 68(9), 2081-2093.

Novosel, I., Spence, G.D., Hyndman, R.D., 2005. Reduced magnetization produced by increased methane flux at a gas hydrate vent. *Marine Geology* 216(4), 265-274.

Ojha, P.S., Dubey, M., 2006. Giant hydrocarbons fields of offshore Krishna-Godavari basin, Petroview 1. Directorate General of Hydrocarbons, New Delhi, 26-30.

Peketi, A., Mazumdar, A., Joshi, R.K., Patil, D.J., Srinivas, P.L., Dayal, A.M., 2012.

Tracing the Paleo sulfate-methane transition zones and H₂S seepage events in marine sediments: An application of C-S-Mo systematic. *Geochemistry Geophysics Geosystems* 13, Q10007. doi:10.1029/2012GC004288.

Passier, H.F., De Lange, G.J., Dekkers, M.J., 2001. Magnetic properties and geochemistry of the active oxidation front and the youngest sapropel in the eastern Mediterranean Sea. *Geophysical Journal International* 145(3), 604-614.

Peketi, A., Mazumdar, A., Joshi, R.K., Patil, D.J., Srinivas, P.L., Dayal, A.M., 2012. Tracing the paleo sulfate-methane transition zones and H₂S seepage events in marine sediments: an application of C-S-Mo systematics. *Geochemistry Geophysics Geosystems* 13(10), Q10007. doi: 10.1029/2012GC004288.

Petersen, N., von Dobeneck, T., Vali, H., 1986. Fossil bacterial magnetite in deep-sea sediments from the South Atlantic Ocean. *Nature* 320, 611-615. doi: 10.1038/320611a0.

Poulton, S.W., Krom, M.D., Raiswell, R., 2004. A revised scheme for the reactivity of iron (oxyhydr) oxide minerals towards dissolved sulfide. *Geochimica et Cosmochimica Acta* 68(18), 3703-3715.

Powell, C.McA. Roots, S.R., Veevers, J.J., 1988. Pre-breakup continental extension in East Gondwanaland and the early opening of the eastern Indian Ocean. *Tectonophysics* 155(1-4), 261-283.

Prabhakar, K.N., Zutshi, P.L., 1993. Evolution of southern part of Indian east coast basins. *Journal of Geological Society of India* 41, 215-230.

Ramana, M.V., Nair, R.R., Sarma, K.V.L.N.S., Ramprasad, T., Krishna, K.S., Subrahmanyam, V., D'Cruz, M., Subrahmanyam, C., Paul, J., Subrahmanyam, A.S., Chandra Sekhar, D.V., 1994. Mesozoic anomalies in the Bay of Bengal. *Earth and Planetary Science Letters* 121(3-4), 469-475.

Ramana, M.V., Ramprasad, T., Kamesh Raju, K.A., Desa, M., 2007. Occurrence of gas hydrates along the continental margins of India, particularly the Krishna-Godavari offshore basin. *International Journal of Environmental Studies* 64(6), 675-693.

Ramana, M.V., Ramprasad, T., Paropkari, A.L., Borole, D.V., Rao, B.R., Karisiddaiah, S.M., Desa, M., Kocherla, M., Joao, H.M., Lokabharati, P., Gonsalves, M.J., Pattan, J.N., Khadge, N.H., Prakash Babu, C., Sathe, A.V., Kumar, P., Sethi, A. K., 2009. Multidisciplinary investigations exploring indicators of gas hydrate occurrence in the Krishna-Godavari basin offshore, east coast of India. *Geo-Marine Letters* 29, 25-38.

Riedel, M., Collett, T.S., Kumar, P., Sathe, A.V., Cook A., 2010. Seismic imaging of a fractured gas hydrates system in the Krishna-Godavari Basin offshore India. *Marine and Petroleum Geology* 27(7), 1476-1493.

- Riedinger, N., Pfeifer, K., Kasten, S., Garming, J.F.L., Vogt, C., Hensen, C., 2005. Diagenetic alteration of magnetic signals by anaerobic oxidation of methane related to a change in sedimentation rate. *Geochimica et Cosmochimica Acta* 69(16), 4117-4126.
- Roberts A.P., Pillans, B.J., 1993. Rock magnetism of lower/middle Pleistocene marine sediments, Wanganui basin, New Zealand. *Geophysical Research Letters* 20(9), 839-842.
- Roberts, A.P., Turner, G.M., 1993. Diagenetic formation of ferrimagnetic iron sulphide minerals in rapidly deposited marine sediments, South Island, New Zealand. *Earth and Planetary Science Letters* 115(1-4), 257-273.
- Roberts, A.P., 1995. Magnetic properties of sedimentary greigite (Fe₃S₄). *Earth and Planetary Science Letters* 134(3-4), 227-236.
- Roberts, A.P., Reynolds, R.L., Verosub, K.L., Adam, D.P., 1996. Environmental magnetic implications of greigite (Fe₃S₄) formation in a 3 m.y. lake sediment record from Butte Valley, northern California. *Geophysical Research Letters* 23(20), 2859-2862.
- Roberts, A.P., Jiang, W.T., Florindo, F., Horng, C.S., Laj, C., 2005. Assessing the timing of greigite formation and the reliability of the Upper Olduvai polarity transition record from the Crostolo River, Italy. *Geophysical Research Letters* 32(5), L05307. doi: 10.1029/2004GL022137.
- Roberts, A.P., Weaver, R., 2005. Multiple mechanisms of remagnetization involving sedimentary greigite (Fe₃S₄). *Earth and Planetary Science Letters* 231(3-4), 263-277
- Rowan, C.J., Roberts, A.P., 2006. Magnetite dissolution, diachronous greigite formation, and secondary magnetizations from pyrite oxidation: unravelling complex magnetizations in Neogene marine sediments from New Zealand. *Earth and Planetary Science Letters* 241(1-2), 119-137.
- Rowan, C.J., Roberts, A.P., Broadbent, T., 2009. Reductive diagenesis, magnetite dissolution, greigite growth and paleomagnetic smoothing in marine sediments: a new view. *Earth and Planetary Science Letters* 277(1-2), 223-235.
- Sagnotti, L., Roberts, A. P., Weaver, R., Verosub, K.L., Florindo, F., Pike, C.R., Clayton, T., Wilson, G.S., 2005. Apparent magnetic polarity reversals due to remagnetization resulting from late diagenetic growth of greigite from siderite. *Geophysical Journal International* 160(1), 89-100.
- Scotese, C.R., Gahagan, L.M., Larson, R.L., 1988. Plate tectonic reconstructions of the Cretaceous and Cenozoic ocean basins. *Tectonophysics* 155(1-4), 27-48.
- Singh, S.C., Minshull, T.A., Spence, G.D., 1993. Velocity structure of a gas hydrate reflector. *Science* 260, 204-207.
- Sloan, E.D., 1990. *Clathrate hydrates of natural gases*, Marcel Dekker, Inc., New York. 641pp.
- Snowball, I., Thompson, R., 1990. A stable chemical remanence in Holocene sediments. *Journal of Geophysical Research* 95(B4), 4471-4479.

- Subramanian, V., 1980. Mineralogical input of suspended matter by Indian rivers into the adjacent areas of the Indian Ocean. *Marine Geology* 36(3-4), M29-M34.
- Sweeney, R.E., Kaplan, I.R., 1973. Pyrite framboid formation; laboratory synthesis and marine sediments. *Economic Geology* 68(5), 618-634.
- Tarduno, J.A., 1995. Superparamagnetism and reduction diagenesis in pelagic sediments: enhancement or depletion? *Geophysical Research Letters* 22(11), 1337-1340.
- Teichert, B.M.A., Eisenhauer, A., Bohrmann, G., Haase-Schramm, A., Bock, B., Linke, P., 2003. U/Th systematics and ages of authigenic carbonates from Hydrate Ridge, Cascadia Margin: recorders of fluid flow variations. *Geochimica et Cosmochimica Acta* 67(20), 3845-3857.
- Thompson, R., Oldfield, F., 1986. *Environmental magnetism*, Allen and Unwin., London. 227pp.
- Torii, M., Fukuma, K., Horng, C.S., Lee, T.Q., 1996. Magnetic discrimination of pyrrhotite-and greigite-bearing sediment samples. *Geophysical Research Letters* 23(14), 1813-1816.
- Torres, M.E., Brumsack, H.J., Bohrmann, G., Emeis, K.C., 1996. Barite fronts in continental margin sediments: a new look at barium remobilization in the zone of sulfate reduction and formation of heavy barites in diagenetic fronts. *Chemical Geology* 127(1-3), 125-139.
- Tric, E., Laj, C., Jéhanno, C., Valet, J.P., Kissel, C., Mazaud, A., Iaccarino, S., 1991. High-resolution record of the Upper Olduvai transition from Po Valley (Italy) sediments: support for dipolar transition geometry? *Physics of the Earth and Planetary Interiors* 65(3-5), 319-336.
- Tudryn, A., Tucholka, P., 2004. Magnetic monitoring of thermal alteration for natural pyrite and greigite. *Acta Geophysica Polonica* 52(4), 509-520.
- Tyson, R. V., 1995. *Sedimentary organic matter: organic facies and palynofacies*, Chapman and Hall., New York. 615pp.
- Ussler III, W., Paull, C.K., 2008. Rates of anaerobic oxidation of methane and authigenic carbonate mineralization in methane-rich deep-sea sediments inferred from models and geochemical profiles. *Earth and Planetary Science Letters* 266, 271-287. doi:10.1016/j.epsl.2007.10.056.
- Verosub, K.L., Roberts, A.P., 1995. *Environmental magnetism: past, present and future*. *Journal of Geophysical Research* 100(B2), 2175-2192.
- Wilkin, R.T., Barnes, H.L., 1997. Formation processes of framboidal pyrite. *Geochimica et Cosmochimica Acta* 61(2), 323-339.
- Worm, H.U., Clark, D., Dekkers, M.J., 1993. Magnetic susceptibility of pyrrhotite: grain size, field and frequency dependence. *Geophysical Journal International* 114(1), 127-137.

Figures caption:

Figure 1. a) Location map of the study area in Krishna Godavari offshore basin, eastern continental margin of India. The star denotes the location of the studied core obtained onboard R/V *Marion Dufresne* (MD161). The inset shows the zoom out of the study area. The contour interval is 50 m. b) Seismic section across the studied core highlighting the presence of a BSR. The thick black line indicates the length of the core NGHP-01-10 and the blue lines indicates the length of the core MD161/8.

Figure 2. Environmental magnetic parameters representing composition and concentration such as χ , SIRM, ARM, soft-IRM, hard-IRM, and S-ratio are shown. The wet-bulk density measured onboard R/V *Marion Dufresne* using GeoTek Multi-Sensor Core Logger is shown for comparison. Three prominent zones (*zone 1*, *zone 2* and *zone 2a*) representing distinct magnetic properties are shown.

Figure 3. The magnetic granulometry parameters such as ARM/SIRM, frequency- dependent magnetic susceptibility [$\chi_{fd}(\%)$], SIRM/ χ are shown. The low-frequency mass specific magnetic susceptibility (solid black curve) measured in laboratory is plotted along with the volume-based magnetic susceptibility (solid red curve) measured onboard R/V *Marion Dufresne* (MD161) for comparison.

Figure 4. The magnetic susceptibility measured during heating (black) and cooling (red) cycles are shown for selected samples from different *zones*. The observed Curie temperatures (350-450 °C) is attributed to the titanomagnetite with varying amount of Ti. The abrupt increase in magnetic susceptibility when the samples are heated beyond 400 °C is attributed to the presence of pyrite. Cooling curves are different from the heating curves suggesting the change is mineralogy during heating.

Figure 5. The hysteresis loops for selected samples from different zones are shown. Beyond 8 mbsf, the hysteresis loop hardly opens suggesting significant presence of paramagnetic mineral pyrite.

Figure 6. The SEM images of magnetic extracts from different depths are shown. The arrows indicate dissolution of the magnetic grains. A) The dissolution of titanomagnetite (TM) crystal is clearly observed at 6.84 mbsf. B) Dissolution of larger titanomagnetite grain is observed at 10 mbsf. C and D) Complex dissolution pattern of titanohaematite (TH) grains is observed.

Figure 7. The SEM images of the magnetic extracts from different depths are shown. A) Pyrite framboid at ~11.16 mbsf. B) Pyrite crystals from *zone 2a* (at 20.73 mbsf) C) and D) show the zoom outs

of pyrite crystals (at 20.73 mbsf) which are filled with fine-grained diagenetic greigite. The alphabets “P” and “G” refer to pyrite and greigite, respectively.

Figure 8. The XRD analysis of magnetic extracts from different depths. A) XRD peaks at 0.54 mbsf (*zone 1*) correspond to titanomagnetite (marked as TM). B) XRD peaks at 18.72 mbsf (*zone 2a*) correspond to pyrite (marked as P). C) XRD peaks at 20.08 mbsf (*zone 2a*) correspond to a mixture of pyrite and greigite (marked as G). The peak corresponding to quartz (marked as Q) is present in all the samples.

Figure 9. Low-temperature magnetic measurements for selected samples in *zone 2a*. Plots A, B, and C represent the thermal demagnetization curves of 2.5T IRM imparted on samples at 10° K (ZFC is represented by black diamonds) and (FC is represented by black circles). Plots E, F, and G represent the low-temperature cycling curves of 2.5T IRM imparted on samples at room temperature (RTSIRM). The cooling curves are shown as cross while the warming curves are shown as star.

Figure 10. The temperature and frequency variations of magnetic susceptibility $\chi(T,f)$ for a selected sample at 21.36 mbsf (*zone 2a*). A) and B) show the real $\chi'(T,f)$ and imaginary $\chi''(T,f)$ components which indicate strong frequency dependent properties suggesting the presence of superparamagnetic domain ferrimagnetic particles. C) shows the reciprocal of the real component ($1/\chi$) which highlights the effect of paramagnetic and ferrimagnetic particles.

Figure 11. The pore water and CRS profiles of the core. A) Low-frequency magnetic susceptibility. B) Pore-water sulfate profile (redrawn from Mazumdar et al., 2009). The present day SMTZ is highlighted by a double-arrow. C) CRS profile (redrawn from Peketi et al., 2012).

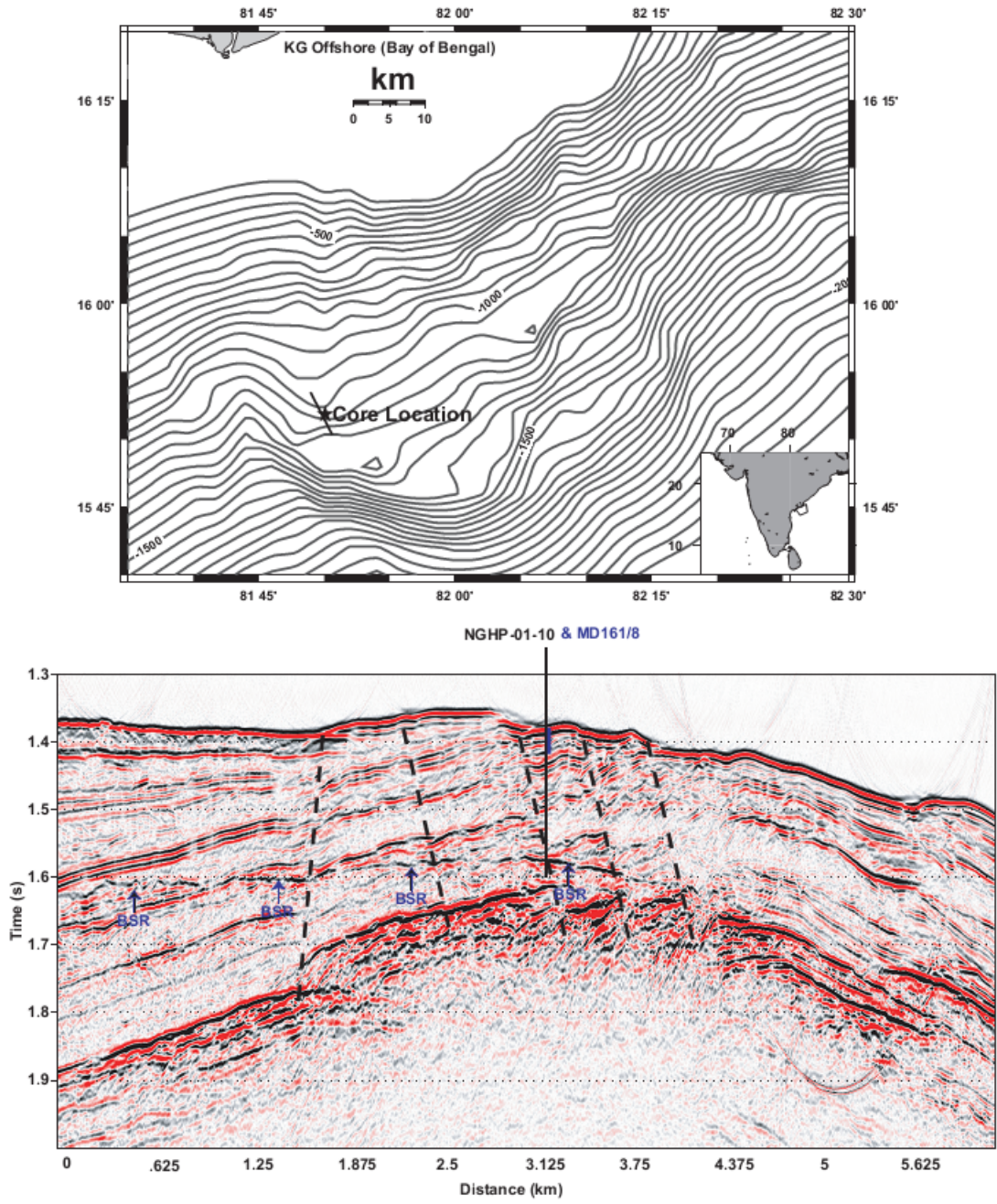


Figure 1

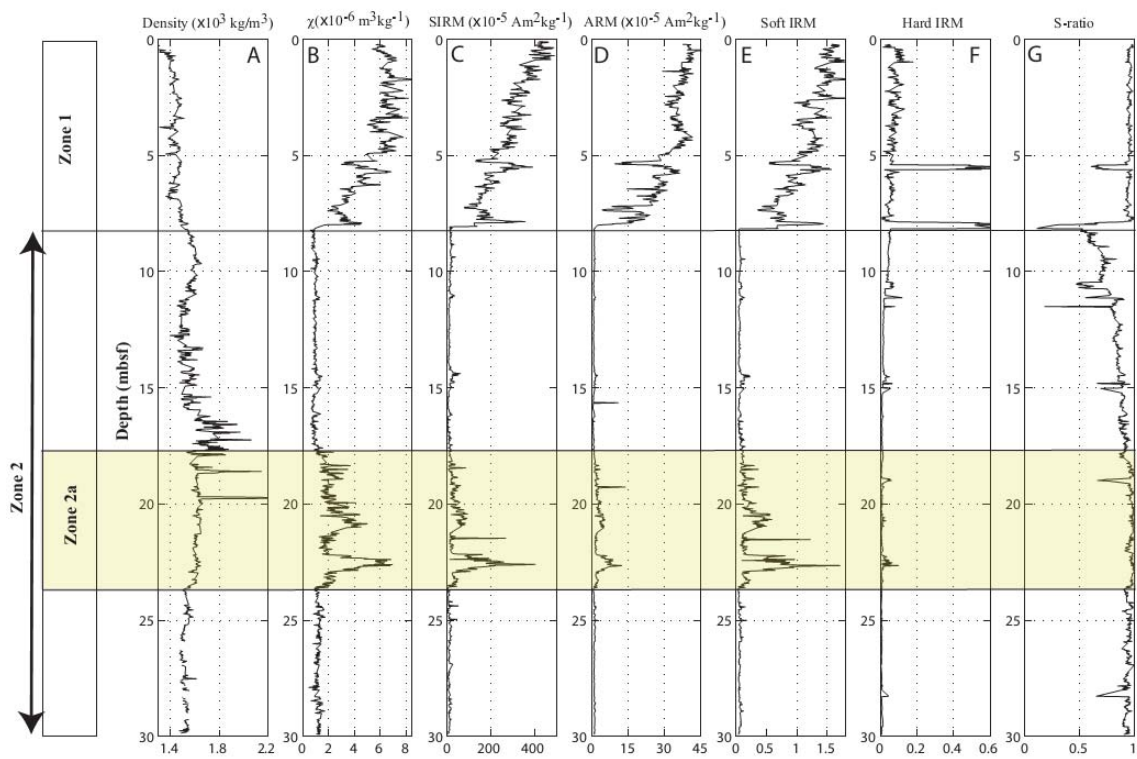


Figure 2

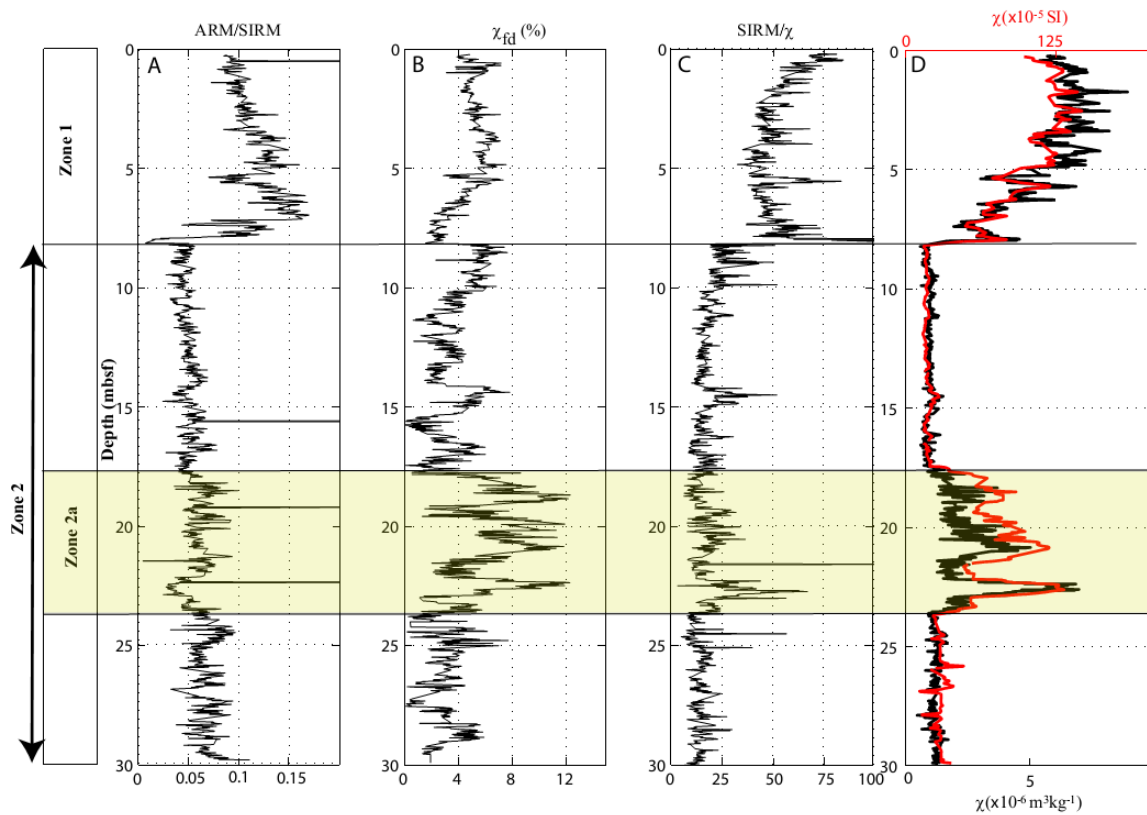


Figure 3

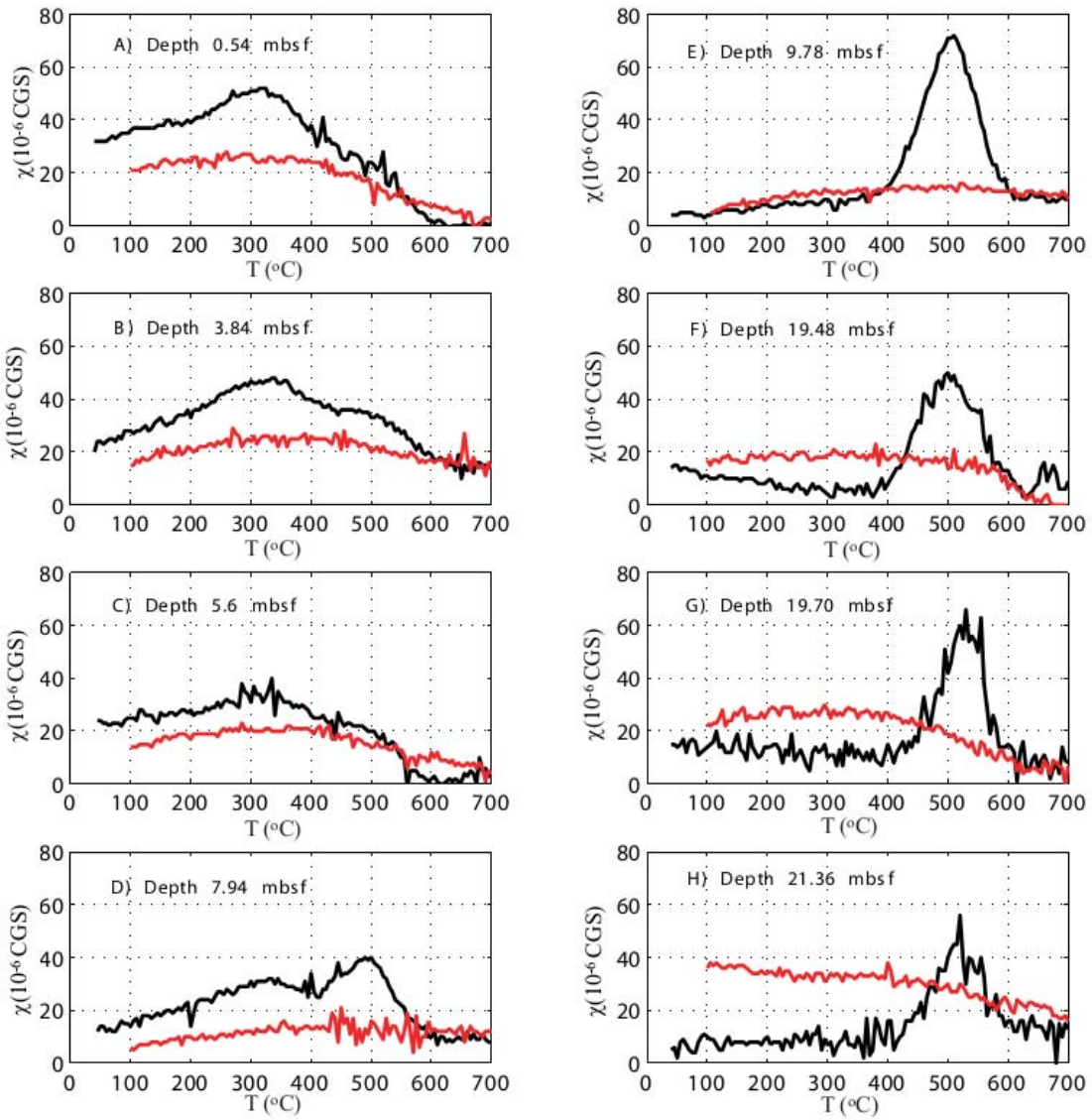


Figure 4

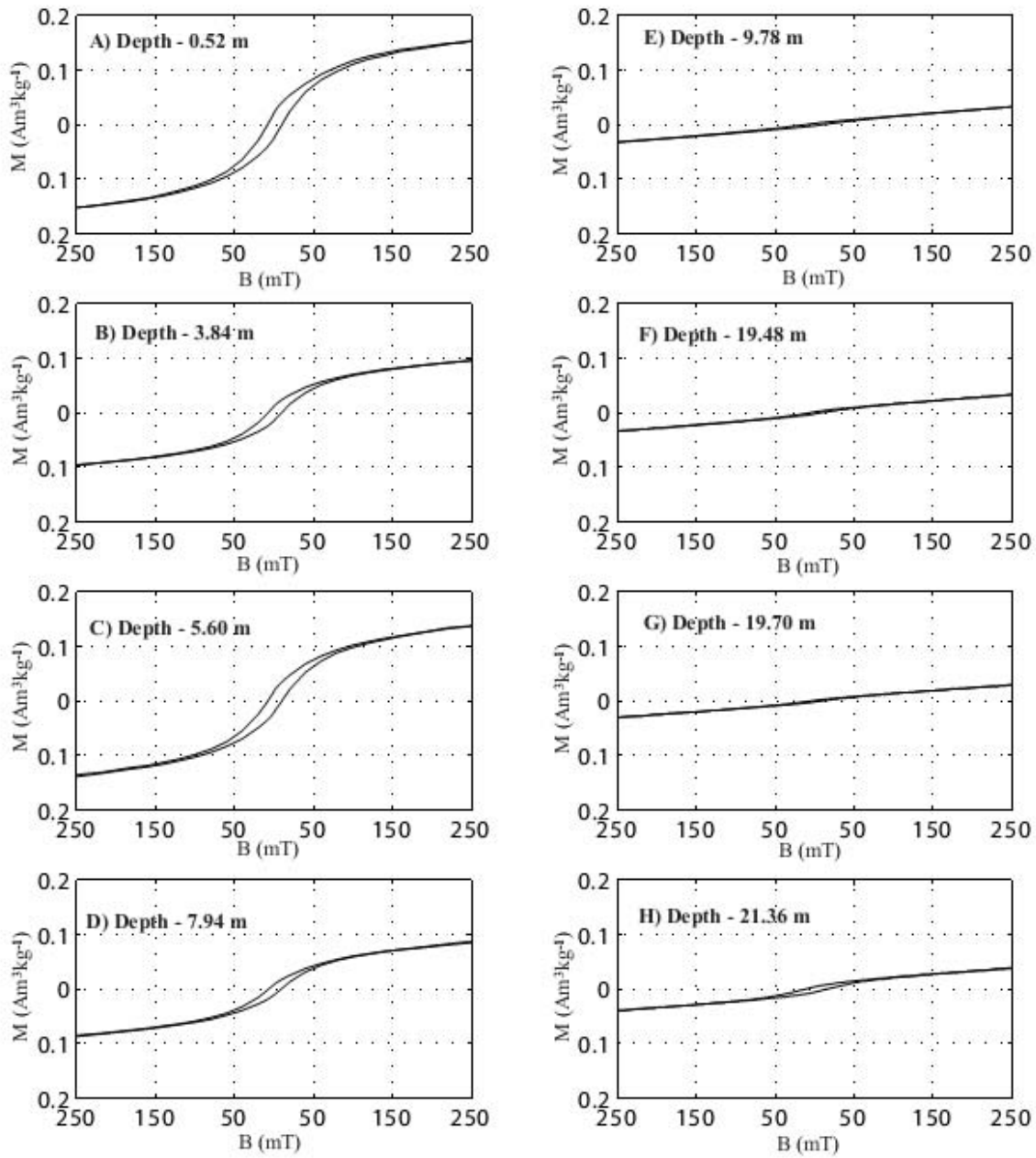


Figure 5

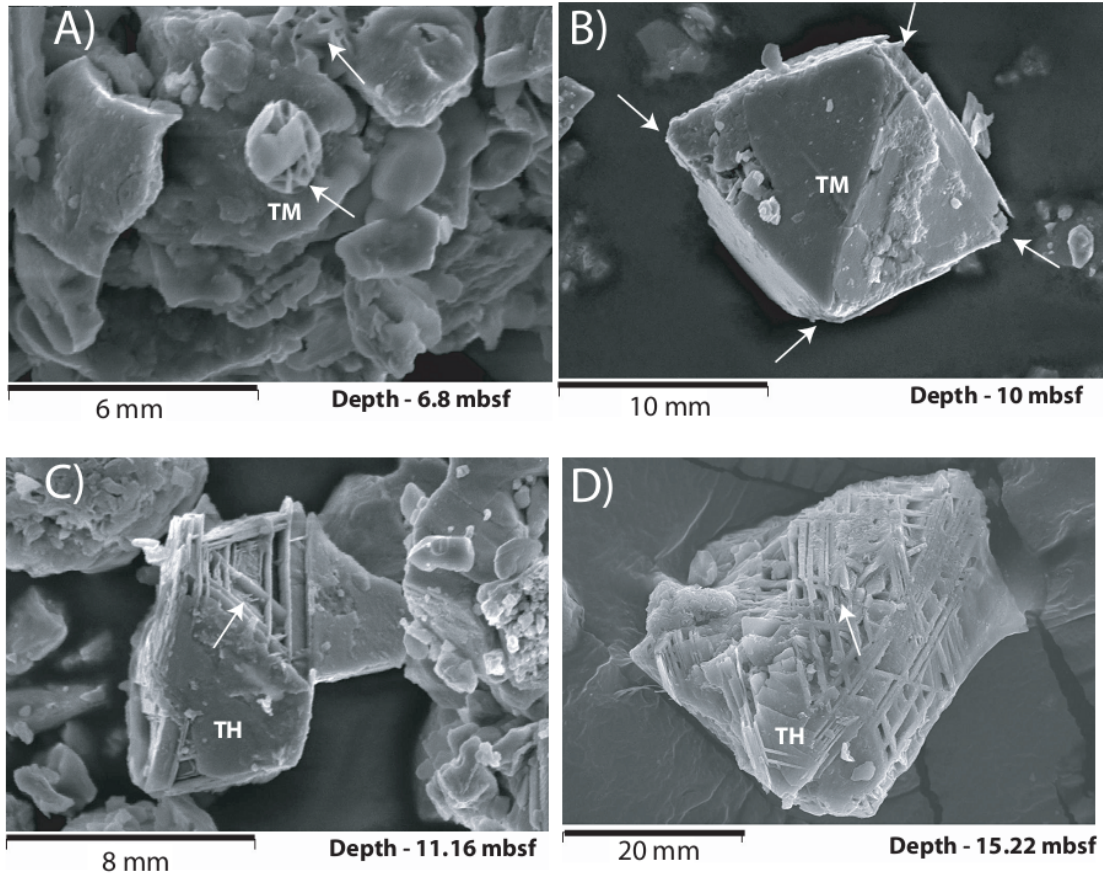


Figure 6

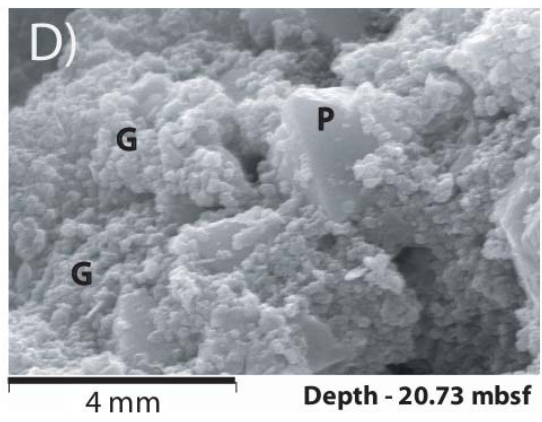
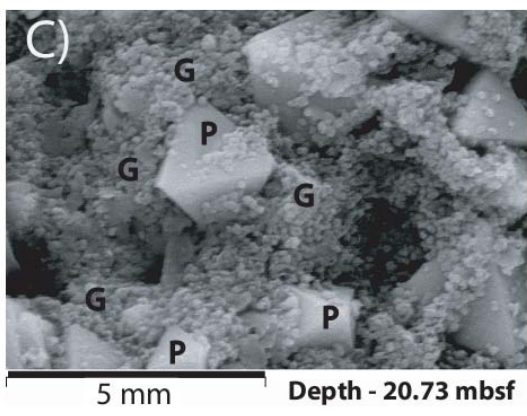
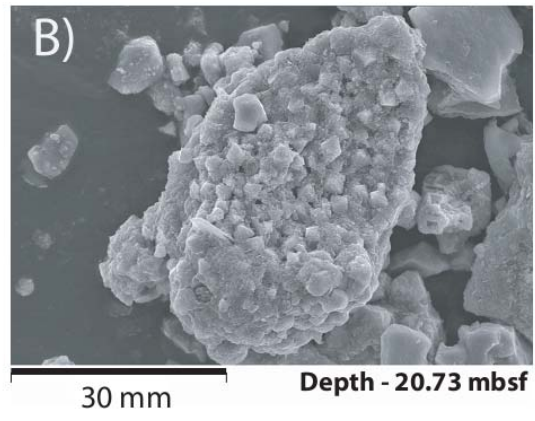
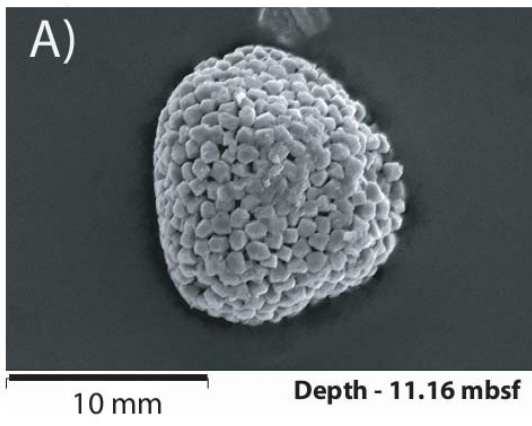


Figure 7

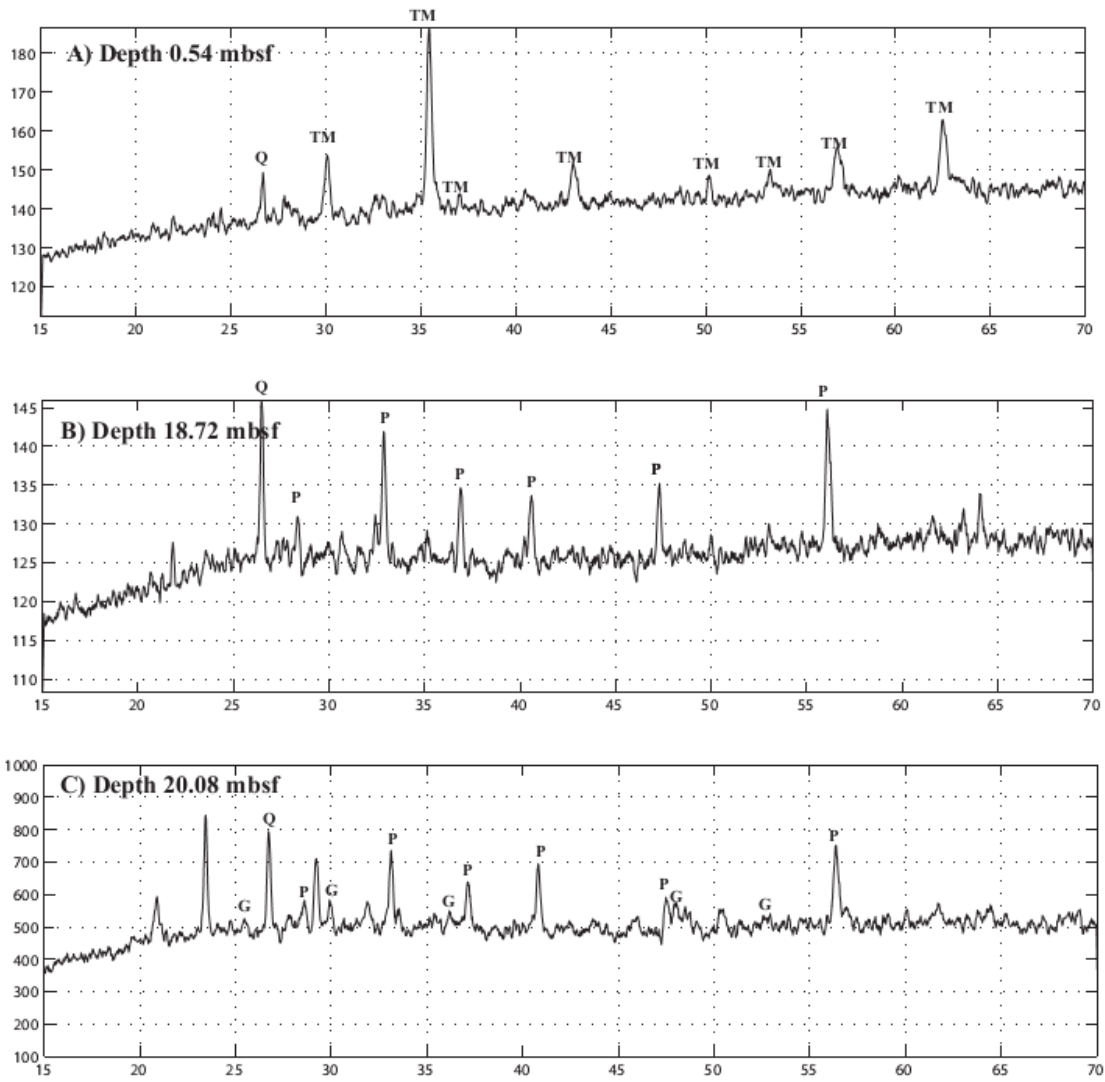


Figure 8

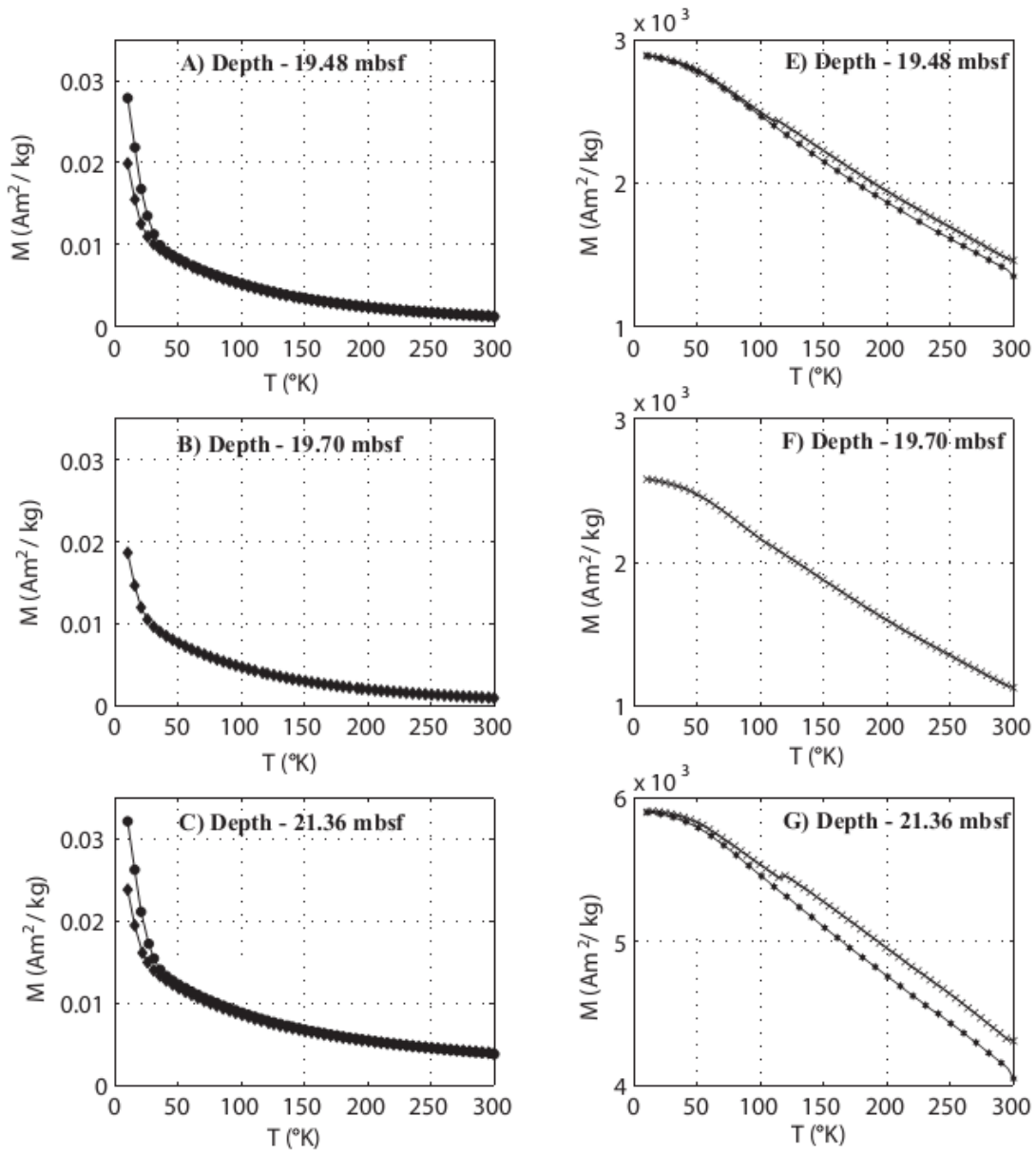


Figure 9

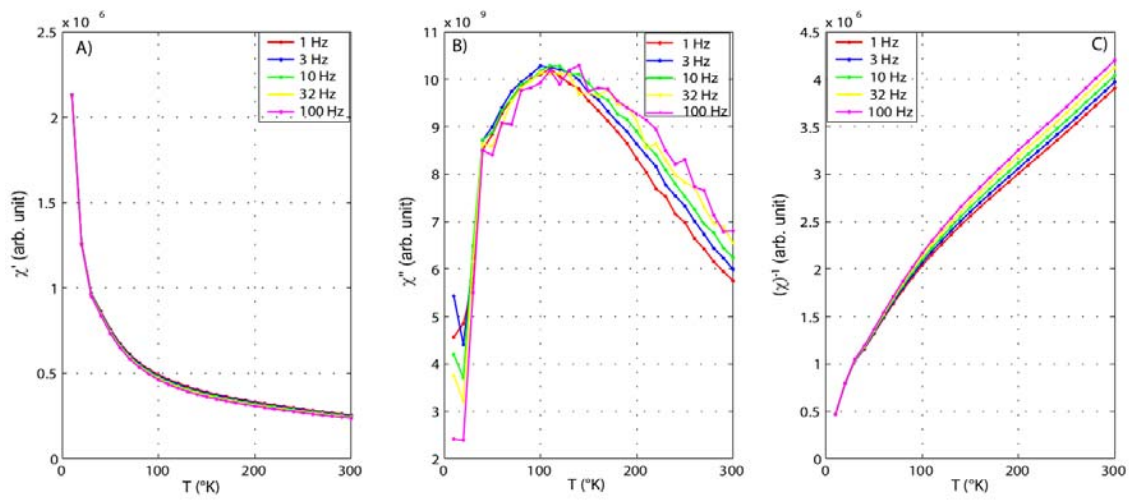


Figure 10

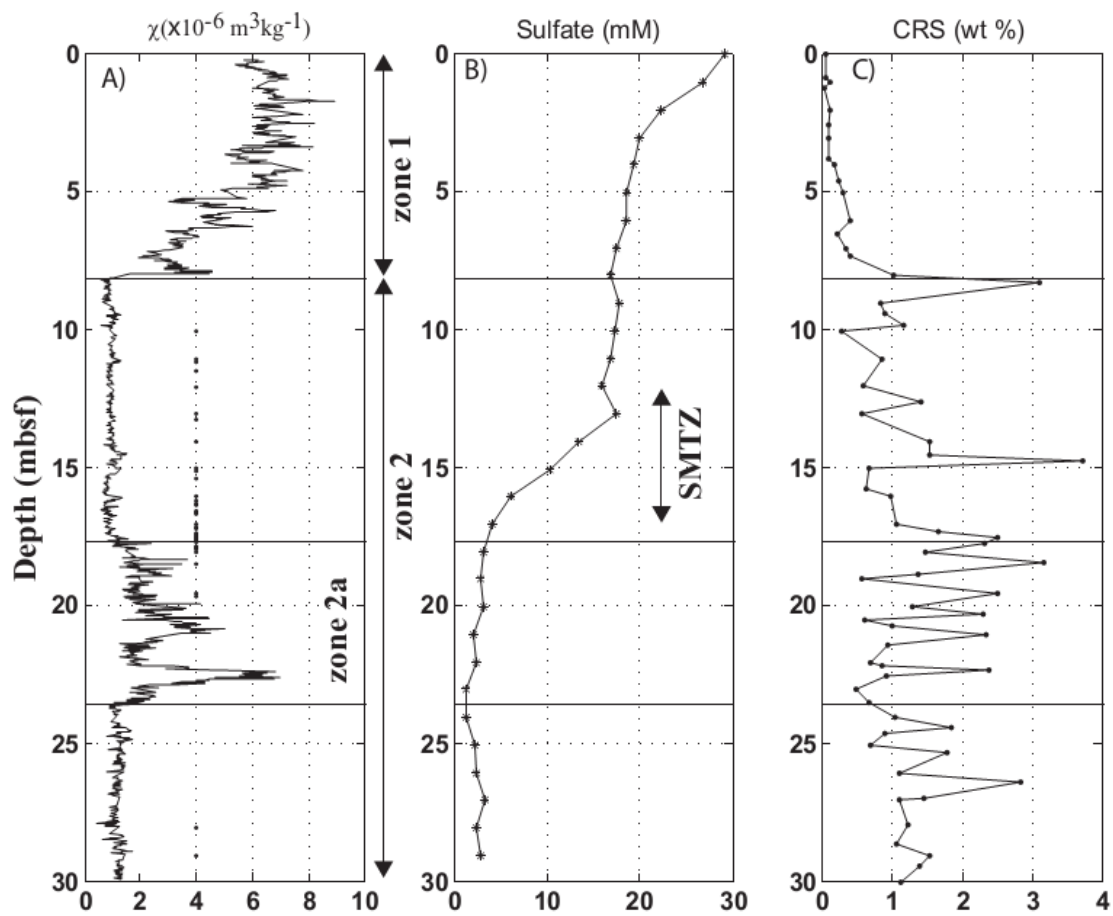


Figure 11